Akizawa *et al.*
Progress in Earth and Planetary Science (2023) 10:30
https://doi.org/10.1186/s40645-023-00560-4

Progress in Earth and Planetary Science

RESEARCH ARTICLE Open Access

Formation of lower fast-spread oceanic crust: a structural and geochemical study of troctolites in the Hess Deep Rift (East Pacific Rise)

Norikatsu Akizawa[1,2*], Marguerite Godard[3], Benoît Ildefonse[3] and Shoji Arai[4]

Abstract

Troctolites were recovered during Integrated Ocean Drilling Program Expedition 345 at the Hess Deep Rift, next to fast-spreading East Pacific Rise. These troctolites are divided into three groups based on textural differences: coarse-grained (1–10 mm in length) troctolite, fine-grained (~ 2 mm in length) troctolite, and skeletal olivine-bearing troctolite. All troctolites exhibit a magmatic fabric. The major-element compositions of olivine, plagioclase, and clinopyroxene in the troctolites are intermediate between those of Hess Deep gabbros and harzburgites. The trace-element compositions of olivine, plagioclase, and clinopyroxene in the troctolites overlap with those of troctolites from slow-spread crust, but they record no petrographic evidence indicating assimilation of mantle peridotite. Thermodynamic calculation for mineral chemistry showed that fractional crystallization of melt is the dominant process responsible for the formation of the troctolites. The fine-grained troctolite was crystallized with high crystallization rate resulting from hot melt injection into colder wall gabbro. In contrast, interactions between the unsolidified troctolite containing interstitial melt and newly injected melt resulted in the formation of the skeletal olivine-bearing troctolite. While our results demonstrate that the troctolites exhibit multiple melt injections and partial dissolution of a troctolite precursor, fractional crystallization is the dominant process for the creation of the lower crust in the Hess Deep Rift.

Keywords IODP expedition 345, Lower oceanic crust, Fractional crystallization, Mid-ocean ridge basalt, Porous melt migration, Melt-mantle interaction

1 Introduction

Fractional crystallization is considered to be the dominant process that influences the compositional characteristics of mid-ocean ridge basalts (MORBs). However, there are a number of processes that complicate this simple picture. Multiple crystallization in the mantle and crust levels (Grove et al. 1993; Herzberg 2004), assimilation of crustal rocks (De Paolo 1981; Michael and Schilling 1989; Freund et al. 2013), and porous flow reaction between ascending melts and ambient mantle (e.g., Collier and Kelemen 2010)/lower crust (Philpotts et al. 1999; Philpotts and Dickson 2000; Lissenberg et al. 2013; Lissenberg and MacLeod 2016; Lissenberg et al. 2019; Sanfilippo et al. 2020; Zhang et al. 2021; Ferrando et al. 2021) are the processes that may influence the compositions of MORBs. The lower oceanic crust, which is composed of gabbroic rocks, records the history of primitive magma migration that leads to the gabbroic rock formation, as well as the chemical evolution of the magma. Structural and chemical investigations of the gabbroic rocks are thus essential for elucidating early stage of the magmatic

*Correspondence:
Norikatsu Akizawa
akizawa@aori.u-tokyo.ac.jp
[1] Atmosphere and Ocean Research Institute, University of Tokyo, 5-1-5 Kashiwanoha, Kashiwa, Chiba 277-8564, Japan
[2] School of Natural Sciences, Macquarie University, Balaclava Road, Sydney, NSW 2109, Australia
[3] Géosciences Montpellier, Université de Montpellier, CNRS, Montpellier, France
[4] Department of Earth Sciences, Kanazawa University, Kakuma, Kanazawa 920-1192, Japan

process occurring in the mid-ocean ridges. In this context, troctolite, the most primitive lithology among the gabbroic rocks, is a key for investigating the primitive magma evolution in the mid-ocean ridge.

To date, troctolite samples have been collected from diverse mid-ocean ridge systems, including the East Pacific Rise (e.g., Vanko and Batiza 1982; Hekinian et al. 1993; Perk et al. 2007; Lissenberg et al. 2013), the Southwest Indian Ridge (e.g., Dick et al. 2000, 2002; Zhang et al. 2021; Boulanger et al. 2021), the Mid-Atlantic Ridge (e.g., Cannat et al. 1997; Dick et al. 2008; Drouin et al. 2009, 2010; Godard et al. 2009; Blackman et al. 2011; Ferrando et al. 2018, 2020), and the Mid-Cayman Rise (Elthon 1987). In addition, troctolite xenoliths enclosed in the MORBs have been reported from the East Pacific Rise (Ridley et al. 2006) and the Juan de Fuca Ridge (Dixon et al. 1986; Davis and Clague 1990; Smith et al. 1994). However, in-situ sampling of troctolites in the lower fast-spread crust had rarely been achieved because of the overlying upper oceanic crustal rocks as well as other gabbroic rocks.

The Hess Deep Rift is one of the best places for investigating the magmatic processes across the mantle/crust boundary beneath the fast-spreading East Pacific Rise, because the peridotites and reaction products between magma and peridotite have already been drilled at the Hess Deep Rift during Ocean Drilling Program (ODP) Leg 147 (Arai and Matsukage 1996; Dick and Natland 1996). Besides, Integrated Ocean Drilling Program (IODP) Expedition 345 targeted the lower crust formed at the fast-spreading East Pacific Rise exposed at the Hess Deep Rift, and collected more than 100 m of troctolites (Gillis et al. 2014a, b). Using microstructural and geochemical approaches, we investigate the primitive magma evolution driving the formation of troctolites in the lower oceanic crust in the fast-spreading East Pacific Rise.

2 Tectonic and geological setting of Hess Deep Rift and troctolite drilled during ODP Leg 147

Hess Deep is the deepest part of the east–west trending Cocos-Nazca rift valley (Fig. 1a), on the eastern flank of the East Pacific Rise (EPR), spreading at a half-rate of 6.5 cm year^{-1} (Lonsdale 1988). It extends 20 km in the east–west direction (Fig. 1b) and deepens to more than 5400 m below sea level (mbsl), while its shoulders rise to less than 2200 mbsl (Francheteau et al. 1990). EPR-derived volcanics, sheeted dikes, and gabbros crop out along the scarps that bound the Hess Deep Rift (northern and southern scarps labeled in Fig. 1b). The sheeted dikes are generally subvertical and strike north–south to northwest-southeast, parallel to the EPR ridge axis (Francheteau et al. 1992; Karson et al. 1992). The formation of the Hess Deep Rift is associated with the westward propagation of the Cocos-Nazca Ridge into the newly formed EPR crust. U–Pb dating of zircon from the gabbroic rocks collected at the Hess Deep Rift constrains their age from 1.420 to 1.271 Myr (Rioux et al. 2012).

The Hess Deep Rift is a unique tectonic window into young fast-spread ocean crust. Rock samples have been successively collected from the lower crust to the upper crust using remotely operated submersible vehicles and drilling (Francheteau et al. 1990, 1992; Hékinian et al. 1993; Gillis et al. 1993; Lissenberg et al. 2013; Gillis et al. 2014a). These samples comprise troctolites, gabbroic rocks, dolerites, and basalts. The upper crustal rock sequence was drilled at ODP Site 894, whereas the lower crustal rock to uppermost mantle rock sequences were drilled at ODP Site 895 (Gillis et al. 1993). Serpentinized mantle peridotites with various modal compositions, such as dunites, wehrlites, and harzburgites have also been collected (Girardeau and Francheteau 1993; Arai and Matsukage 1996; Dick and Natland 1996; Arai and Takemoto 2007).

Troctolites were recovered at ODP Site 895 (marked by the black star in Fig. 1b) during ODP Leg 147. They are 0.5–7 m-thick intervals bounded by the dunites or harzburgites with gradational or sharp boundaries (Gillis et al. 1993). The olivine and plagioclase contents in the troctolites show significant variations, even in the case of a single hand specimen. The troctolites show variable mineral chemistry: 0.5–3.0 wt% TiO_2 in spinel, and 0.2–2.0 wt% TiO_2 and 0.5–2.0 wt% Cr_2O_3 in clinopyroxene (Arai and Matsukage 1996; Dick and Natland 1996). Their structural, petrographic, and mineral chemical variations were attributed to the interactions between percolating melts and the wall harzburgite in the shallow mantle (Arai and Matsukage 1996; Boudier et al. 1996; Dick and Natland 1996). The variable degrees of interactions and melt entrapments produced the observed modal and chemical gradations of the troctolites.

3 IODP expedition 345

IODP Expedition 345 was designed to collect the primitive lower oceanic crust formed at the fast-spreading EPR. IODP Site U1415 (shown by the red star in Fig. 1b) is located on the southern slope of the intra-rift ridge, on a 200 m-wide, flat-lying east–west trending bench (Fig. 1c). The bench is part of an overall lobate structure, which was imaged based on near-bottom bathymetry data acquired during site survey cruise JC21 (RRS James Cook), and is ascribed to mass wasting (Ferrini et al. 2013). A total of 16 holes were drilled at Site U1415 (Gillis et al. 2014a), and three of them were used in this study: one single-bit hole (U1415I) and two reentry holes (U1415J and U1415P).

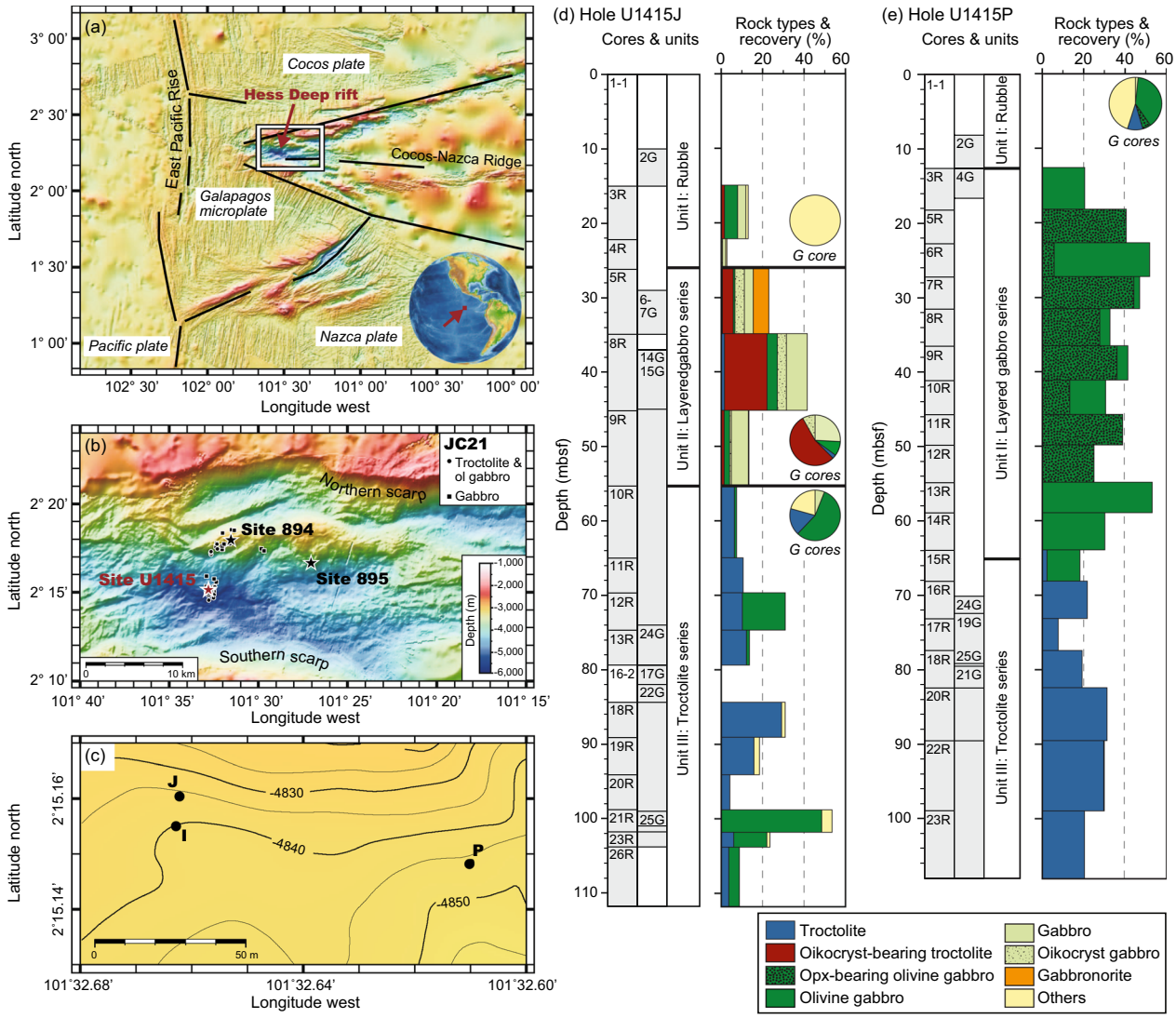

Fig. 1 Geological context. **a** Bathymetric map of the Galapagos triple junction in the eastern equatorial Pacific Ocean highlighting major tectonic boundaries. The white box indicates the location of the map in **b**. **b** Regional bathymetric map of the Hess Deep Rift showing the locations of IODP Site U1415 (red star), and ODP Sites 894 and 895 (black stars). The black circles and squares indicate the sampling localities of RRS James Cook cruise JC21. **c** Micro-bathymetric map showing the locations of Holes U1415I, U1415J and U1415P. **d**, **e** Lithostratigraphic columns of Holes U1415J and U1415P. The columns show depths (mbsf), core numbers, lithological units, rock types, and recovery (%). Lithological units (Units 1 to 3) were identified on the basis of downhole changes in lithology and inclination of magnetization direction. Ghost cores (G cores) are material recovered during hole cleaning operations. The bathymetry in **a**, **b** is derived from satellite altimetry data, and multibeam bathymetry data available from the Global Multi-Resolution Topography Data Portal at the Lamont-Doherty Earth Observatory. Modified from Gillis et al. (2014b). *Opx* Orthopyroxene

The drill cores are mainly composed of gabbroic rocks and troctolites (Fig. 1d, e). The downhole changes in the inclination of the magnetization direction and lithology revealed that the two reentry holes of U1415J and U1415P sampled several coherent faulted blocks, which were displaced by mass wasting (Gillis et al. 2014a). These blocks are grouped as Unit 2 layered gabbro series and Unit 3 troctolite series labeled in Fig. 1d, e.

4 Sample description

A total of 25 troctolites were selected from Holes U1415I, U1415J, and U1415P for this study (Table 1). The samples were classified into three groups based on their textural characteristics: coarse-grained troctolite, fine-grained troctolite, and skeletal olivine-bearing troctolite (Fig. 2). For simplicity, the samples are identified by sequential numbers with the classification: CGT1 to 14, FGT1 to 10, and SOBT1 (Table 1).

Table 1 Details of troctolite samples from Hess Deep

Petrography	Hole	Core section	TI (cm)	Rock type	Note	MGS (mm)			Parameters and aquired values by EBSD analysis												T_{REE} (°C)		T_{BKN} (°C)
Sample name						Ol	Pl	SS (μm)	Ol			Pl			Area fraction (%)							1σ	
									N	J	M	N	J	M	NIA	Ol	Pl	Cpx	Opx	IA total			
FGT1	U1415I	4R2	9	FGT	Cpx oikocryst-bearing	2	2	25	34,750	3.26	0.02	3E+05	1.76	0.03	14.8	6.0	45.6	33.6	0.02	85.2			968
FGT2	U1415J	5R1	111	FGT	Cpx oikocryst-bearing	2	2	30	21,426	12.6	0.11	3E+05	2.96	0.05	12.0	4.5	64.7	18.6	0.14	88.0	1182	33	939
FGT3	U1415J	6G1	11	FGT	Cpx oikocryst-bearing	2	2	30	36,392	3.39	0.05	2E+05	2.47	0.05	23.1	8.2	50.7	17.9	0.06	76.9	1201	27	965
FGT4	U1415J	7G1	28	FGT	Cpx oikocryst-bearing	2	2	30	5531	5.91	0.05	1E+05	3.94	0.12	22.6	2.4	58.2	14.8	2.03	77.4	1200	32	976
FGT5	U1415J	8R1	99	FGT	Cpx oikocryst-bearing	2	2	30	38,218	2.97	0.03	3E+05	2.58	0.07	12.8	7.2	59.1	20.6	0.35	87.2	1245	15	901
FGT6	U1415J	8R2	5	FGT	Cpx oikocryst-bearing	2	2	30	52,992	2.28	0.03	3E+05	4.46	0.12	19.9	10.5	62.1	7.6	0.02	80.1			1059
FGT7	U1415J	8R2	45	FGT		2	2	25	60,647	2.38	0.04	3E+05	6.39	0.19	22.8	12.2	64.7	0.4	–	77.2			
SOBT1	U1415J	10R1	20	SOBT		8	2	35	56,313	18.6	0.21	84,155	2.14	0.01	36.0	25.1	37.6	1.3	0.06	64.0			
FGT8	U1415J	10R1	45	FGT		2	2	30	87,192	2.18	0.05	3E+05	2.81	0.10	13.6	18.3	67.3	0.6	0.17	86.4			883
FGT9	U1415J	11R1	29	FGT		2	2	50	28,042	3.33	0.09	1E+05	2.33	0.07	23.3	16.2	59.2	1.3	–	76.7	1196	45	
CGT1	U1415J	13R1	44	CGT		5	4	50	19,237			17,973			73.4	13.7	12.8	–	–	26.6			
FGT10	U1415J	15G1	1	FGT	Cpx oikocryst-bearing	2	2	30	47,640	1.90	0.03	3E+05	2.11	0.04	17.1	9.2	50.4	23.2	0.09	82.9			957
CGT2	U1415J	18R1	77	CGT		5	4	50	5129			1124			94.6	4.2	0.9	0.3	–	5.4			
CGT3	U1415J	18R1	146	CGT		7	4	50	8678			16,232			85.4	5.1	9.5	0.0	–	14.6			
CGT4	U1415J	19R1	15	CGT		4	3																
CGT5	U1415P	16R1	21	CGT		4	3	50	26,390			44,581			62.6	13.9	23.5	0.1	–	37.4			
CGT6	U1415P	16R1	41	CGT		7	6	50	38,691			60,540			41.1	22.6	35.4	0.9	–	58.9			
CGT7	U1415P	18R1	57	CGT		7	5	50	6491			18,869			69.1	7.8	22.8	0.3	–	30.9			
CGT8	U1415P	18R1	98	CGT		5	4																
CGT9	U1415P	21G1	4	CGT	Cpx-rich	10	5	50	28,547			20,965			58.3	16.5	12.1	13.0	–	41.7			
CGT10	U1415P	22R1	7	CGT		6	4	50	3199			49,116			51.8	2.9	45.1	0.2	–	48.2			
CGT11	U1415P	22R1	13	CGT		10	5	50	11,745			30,650			68.6	8.5	22.2	0.7	–	31.4			

Table 1 (continued)

Petrography	Hole	Core section	TI (cm)	Rock type	Note	MGS (mm)			Parameters and aquired values by EBSD analysis										T_{REE} (°C)	T_{BKN} (°C)
Sample name						Ol	Pl	SS (μm)	Ol			Pl			Area fraction (%)						1σ	
									N	J	M	N	J	M	NIA	Ol	Pl	Cpx	Opx	IA total		
CGT12	U1415P	22R1	108	CGT		4	4															
CGT13	U1415P	23R1	118	CGT		7	5	50	10,811			26,755			74.4	7.1	16.9	1.6	–	25.6		
CGT14	U1415P	23R2	41	CGT		8	4	50	17,165			46,402			53.6	12.3	33.2	1.0	–	46.4		

Three coarse-grained troctolites, CGT4, CGT8, and CGT12 are not suitable for fabric analysis by EBSD because of their severe alteration, but we could analyze their primary chemical compostions of minerals. N represents number of grains detected by EBSD analysis. Refer to text for further explanations of J-index (J) and M-index (M). REE-in-plagioclase-clinopyroxene thermometer formulated by Sun and Liang (2017) and two pyroxene thermometer formulated by Brey and Köhler (1990) were applied for temperatrue estimates as T_{REE} and T_{BKN}, respectively

CGT Coarse-grained troctolite, *Cpx* Clinopyroxene, *FGT* Fine-grained troctolite, *IA* Indexed area, *MGS* Maximum grain size, *NIA* Not indexed area, *Ol* Olivine, *Opx* Orthopyroxene, *Pl* Plagioclase, *SOBT* Skeletal ol-bearing troctolite, *SS* Step size of EBSD analysis, *TI* Top interval. -: Not detected

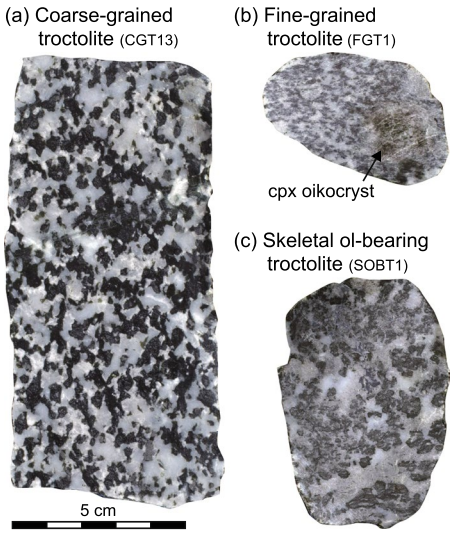

Fig. 2 Photographs of representative troctolites from IODP Site U1415. **a** Coarse-grained troctolite (CGT13). **b** Fine-grained troctolite (FGT1). This type of troctolite includes centimeter-sized clinopyroxene oikocrysts. **c** Skeletal olivine-bearing troctolite (SOBT1). *Ol* Olivine, *Cpx* Clinopyroxene

4.1 Coarse-grained troctolite

14 samples are categorized as coarse-grained troctolites. They all belong to Unit 3 troctolite series in Fig. 1d, e. They contain coarse-grained (1–10 mm in length) olivine and plagioclase, with minor amounts of clinopyroxene and chromian spinel also being present. The olivine is subhedral to anhedral with a subequant habit (aspect ratio = 1:2–1:3), while the plagioclase is subhedral to anhedral with a subequant to tabular habit (aspect ratio = 1:3–1:5). The clinopyroxene is sparse and interstitial to olivine and plagioclase grains (Fig. 3a, b). Subhedral to anhedral chromian spinels are commonly included in the olivine or plagioclase grains (Fig. 3c, d). CGT9 is richer in clinopyroxene (> 10 vol%) with textural features similar to those of the other coarse-grained troctolites (Fig. 3e). The coarse-grained troctolites are severely altered, but the key textural features and minerals are sufficiently preserved such that they were suitable for use in microscopic observations and structural/chemical analyses.

4.2 Fine-grained troctolite

10 samples are categorized as fine-grained troctolites. They were collected from Unit 2 layered gabbro series in Hole U1415J (Fig. 1d), and consist of fine-grained (< 2 mm in length) olivine and plagioclase, with minor interstitial clinopyroxene and orthopyroxene also being present. The fine-grained troctolites are generally well foliated. The olivine is subhedral to anhedral, while the plagioclase is subhedral to anhedral with a subequant to tabular habit (Fig. 3f). 7 of the 10 samples contain centimeter-scale clinopyroxene oikocrysts (Fig. 2b, Table 1). These samples were labelled oikocryst-bearing troctolite by Gillis et al. (2014ab) (Fig. 1d), and studied by Leuthold et al. (2018). The clinopyroxene oikocrysts include euhedral to subhedral plagioclase chadacrysts with an elongated habit (aspect ratio = > 1:5), in sharp contrast to those in the surrounding troctolite matrix. The degree of serpentinization of olivine is much higher closer to the clinopyroxene oikocrysts (Fig. 3g). The olivines close to the clinopyroxene oikocrysts are occasionally rimmed by orthopyroxene, and frequently associated with chemically zoned plagioclase (see color contrast in Fig. 3h).

4.3 Skeletal olivine-bearing troctolite

SOBT1 was collected from Unit 2 layered gabbro series in Hole U1415J (Fig. 1d). It contains olivine exhibiting a "skeletal" morphology, which is associated with partly enclosed plagioclase grains (Fig. 3i). This terminology was used by Gillis et al. (2014a), and is used herein for consistency. Olivines show cuspate and embayed margins (Fig. 3i). Plagioclases are subhedral to anhedral with a subequant to tabular habit (Fig. 3i). Skeletal olivine grains are relatively coarser (< 10 mm in length) than the plagioclase grains (< 8 mm in length). Trace clinopyroxenes are interstitial to olivine and plagioclase grains (Fig. 3i).

5 Analytical methods

We analyzed crystallographic preferred orientation (CPO) and chemical composition of the troctolite samples. We mainly analyzed the core of minerals as the samples are severely altered.

(See figure on next page.)

Fig. 3 Thin section images, photomicrographs, and back-scattered electron images of troctolites from IODP Site U1415. **a**, **g** were taken with plane-polarized light, and **b**, **e**, **f**, **i** were taken with cross-polarized light. **c**, **d**, **h** were taken by EPMA. **a** Coarse-grained troctolite (CGT11). The red square is magnified in **b**. The positions of chromian spinel grains shown in **c**, **d** are pointed by the red arrows. **b** Interstitial clinopyroxene along grain boundaries of olivine and plagioclase in CGT11. **c**, **d** Anhedral and subhedral chromian spinels in CGT11. **e** Interstitial clinopyroxenes in the clinopyroxene-rich coarse-grained troctolite (CGT9). **f** Fine (~ 0.5 mm in long length) olivine grains in the fine-grained troctolite (FGT8). **g** Centimeter-sized clinopyroxene oikocrysts embedded in fine-grained troctolite (FGT10). The red square is magnified in **h**. **h** Partially serpentinized olivine grains rimed with orthopyroxene. **i** Coarse (~ 5 mm in long length) olivine grains exhibit skeletal morphology in the skeletal olivine-bearing troctolite (SOBT1). Clinopyroxenes are interstitial along grain boundaries of olivine and plagioclase, and share the same crystallographic orientation. *Cpx* Clinopyroxene, *Cr-spl* Chromian spinel, *Ol* Olivine, *Opx* Orthopyroxene, *Pl* Plagioclase

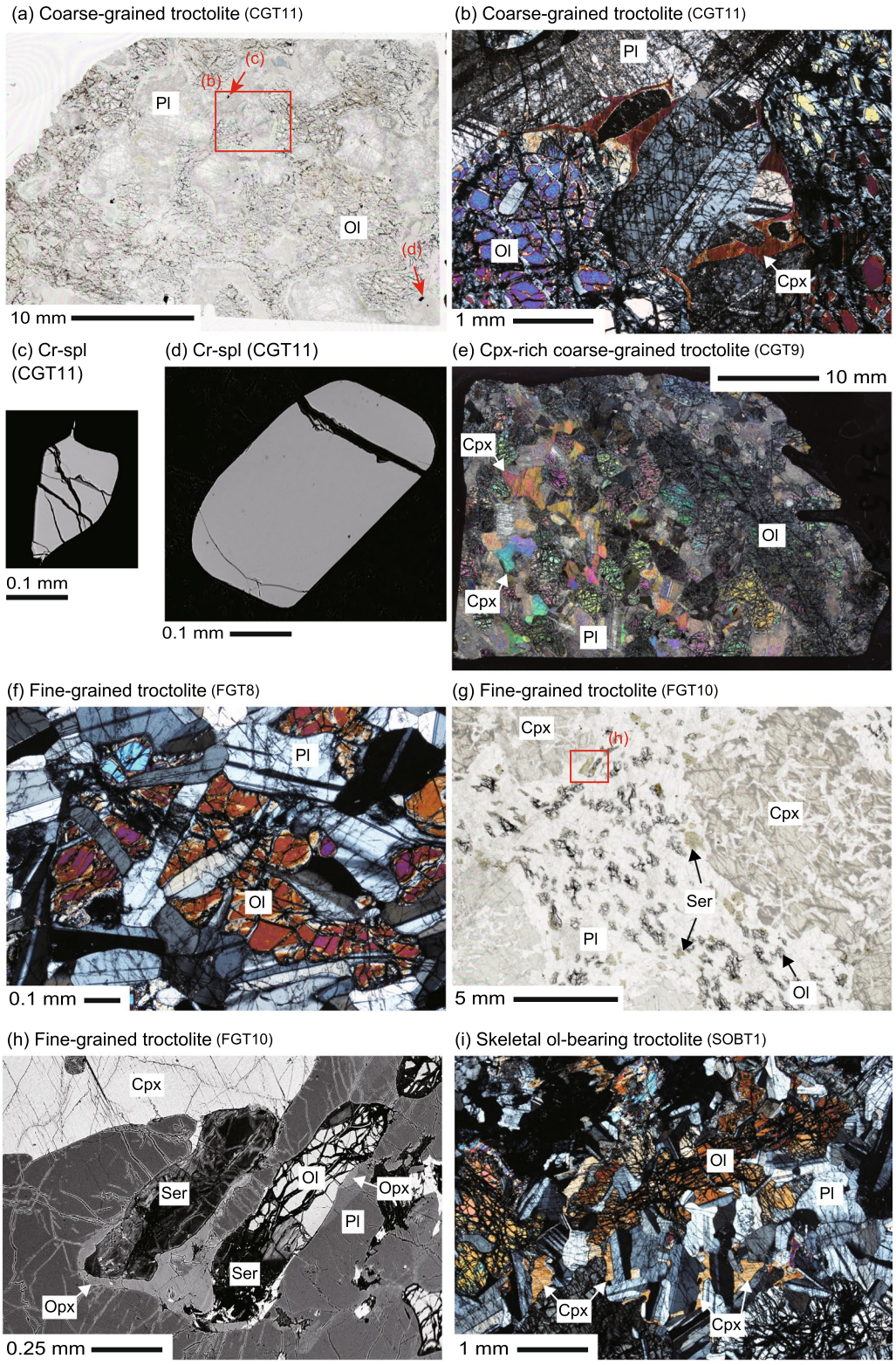

Fig. 3 (See legend on previous page.)

5.1 Crystallographic preferred orientations

CPO measurements were conducted using the electron backscatter diffraction (EBSD) technique (e.g., Prior et al. 2009) at Géosciences Montpellier, University of Montpellier (France). We used a JEOL JSM 5600 scanning electron microscope equipped with Oxford/Nordlys EBSD detectors. Diffraction patterns were collected and processed using the Channel 5® software suite (Schmidt and Olesen 1989). Samples were measured in automatic mode at a regular grid spacing of 25–50 µm over the whole thin sections; indexing rates in the raw maps range from 5 to 88% (see Table 1). A first stage of post-acquisition data processing was conducted using the Tango software of the Channel 5® suite to increase the quality of map data, by (1) removing isolated pixels (either non-indexed, or indexed as a given phase and surrounded by pixels indexed for another phase), (2) filling non-indexed pixels that have a minimum of 5 neighbor pixels with a common phase and orientation with that same orientation, and (3) searching and correcting indexation errors in olivine grains, due to olivine hexagonal pseudosymmetry resulting in similar diffraction patterns for orientations differing by a 60° rotation around [100]. The EBSD data sets were then processed using MTEX (version 5.2.8), a free Matlab toolbox for analyzing and modeling crystallography (http://mtex-toolbox.github.io; Hielscher and Schaeben 2008; Bachmann et al. 2010). We used MTEX to identify grains and produce phase and orientation maps from the EBSD data, calculate pole figures of olivine and plagioclase preferred orientation, and calculate CPO strength and shape indexes. Grains were identified by choosing a 10° threshold, over which the misorientation between two adjacent pixels indexed for the same phase is assumed to be a grain boundary. Grains that have a surface smaller than 5 pixels could be erroneous measurements, and were removed from the data set. Twins in plagioclase were distinguished from grain boundaries by filtering out the boundaries with the relevant misorientation (180°) and rotation axes during the grain boundary identification procedure.

The CPO strength for each phase is determined using both the Orientation Distribution Function (ODF) J-index that is exclusively based on crystallographic orientations (e.g., Bunge 1982; Mainprice and Silver 1993), and the M-index (Skemer et al. 2005), based on the misorientation angle distribution. J varies between 1 (for a uniform distribution) to infinity (for a single crystal); M varies from 0 to 1 (see Mainprice et al. (2015) for the details of J and M calculations, and for a comparison between these two indexes). The ODF was calculated using the "de la Vallee Poussin" kernel with a half width of 10° (Schaeben 1999; Mainprice et al. 2015). Since coarse-grained troctolites and skeletal olivine-bearing troctolite are severely altered and indexed grain numbers are limited for sufficient estimation of ODF, J-index and M-index. Hence, they are calculated only for fine-grained troctolites (Table 1).

5.2 Major-element analysis

Major-element compositions of olivine, plagioclase, clinopyroxene, orthopyroxene, and spinel were analyzed with a JEOL JXA-8800R electron microprobe analyzer (EPMA) at Kanazawa University (Japan). We used an accelerating voltage of 20 kV, a probe current of 20 nA, and a probe diameter of 3 µm, except for plagioclase, for which an accelerating voltage of 15 kV, a probe current of 12 nA, and a probe diameter of 3 µm were used. We used a peak counting time of 30 s, and a background counting time of 10 s except for Ni, for which a peak counting time of 45 s and a background counting time of 15 s were used. Natural and synthetic minerals (quartz, eskolaite, wollastonite, fayalite, jadeite, $KTiPO_5$, corundum, manganosite, periclase and bunsenite) were used as standards. Raw data were corrected using the ZAF online correction program. All Fe was assumed to be ferrous iron (Fe^{2+}) in silicates, and Fe^{2+} and ferric iron (Fe^{3+}) in spinel were calculated assuming spinel stoichiometry. We use Mg# for $Mg/(Mg+Fe^{2+})$ atomic ratio in pyroxenes and spinel, Fo for $100\times Mg\#$ in olivine, An for $Ca/(Ca+Na+K)$ atomic ratio in plagioclase, and Cr# for $Cr/(Cr+Al)$ atomic ratio in spinel.

5.3 Trace-element analysis

Trace-element concentrations (Li, Ti, Ni, Cu, Zn, Rb, Sr, Y, Zr, Nb, Ba, La, Ce, Pr, Nd, Sm, Eu, Gd, Tb, Dy, Ho, Er, Tm, Yb, Lu, Hf, Ta, Pb, Th and U) of olivine, plagioclase, and clinopyroxene were determined at Géosciences Montpellier, University of Montpellier using a Thermo Scientific Element XR (Extended Range) high resolution-inductively coupled plasma-mass spectrometer (HR-ICP-MS) coupled with a MicroLas GeoLas Q-plus 193 nm ArF excimer laser. Ablation experiments were conducted using an in-house modified 30 cm^3 ablation cell with a helium atmosphere to enhance sensitivity and reduce inter-element fractionation (Günther and Heinrich 1999). Each analysis was performed by ablating 77–102 µm in diameter for clinopyroxene, and 122 µm in diameter for olivine and plagioclase. Fresh grains were selected for all the analyses. The laser energy density was set to 10 J/cm^2 per pulse at a frequency of 8 Hz. Data were collected in time resolved acquisition mode: signal integration times were set to 120 s for a gas background interval and 60 s for an ablation interval. Data was quantified with the GLITTER software (Van Achterbergh et al. 2001) using the linear fit to ratio method. Sample concentrations were calibrated against the NIST SRM 612. Element

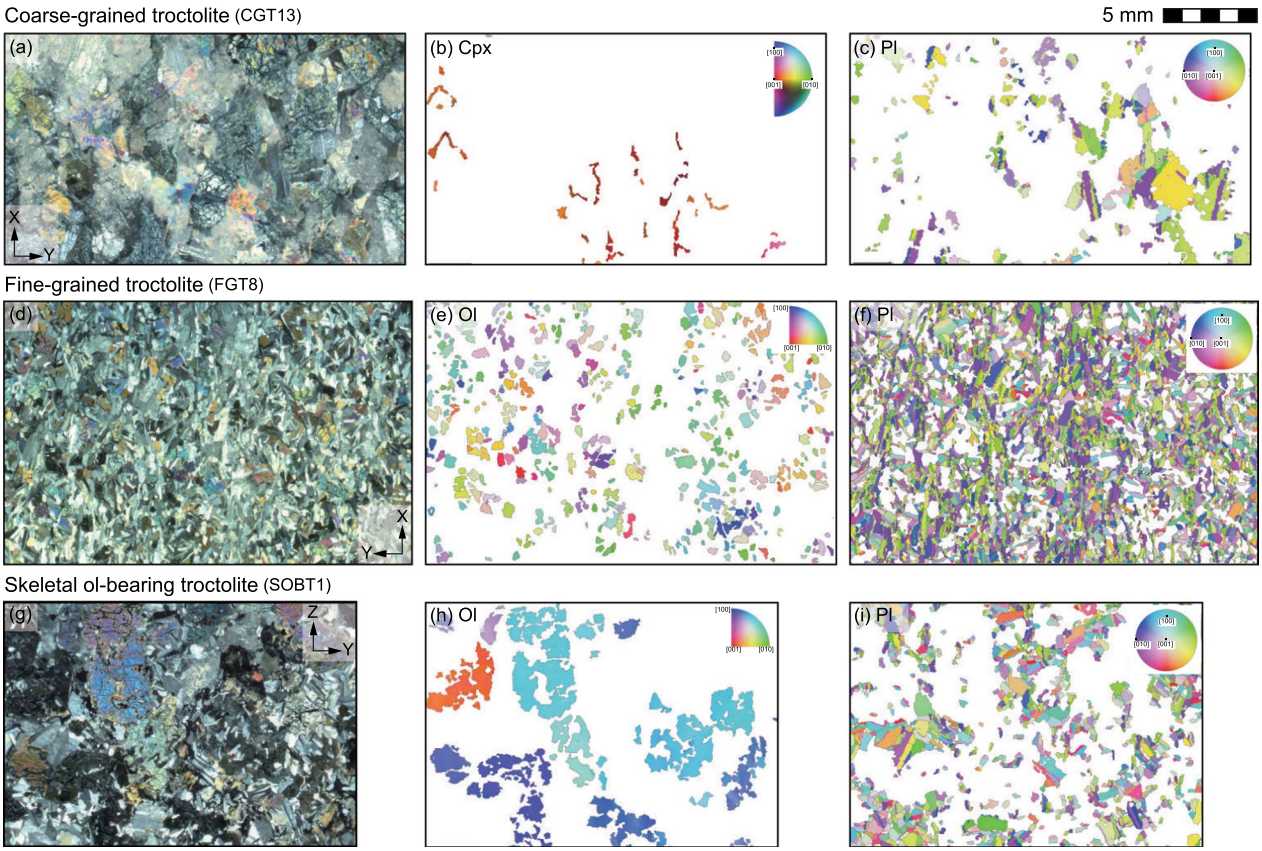

Fig. 4 Thin section images under cross-polarized light (left side) and EBSD inverse pole figure orientation maps (center and right side). **a**–**c** Coarse-grained troctolite. **d**–**f** Fine-grained troctolite. **g**–**i** Skeletal olivine-bearing troctolite

concentrations of the NIST SRM 612 were selected from the preferred values of Pearce et al. (1997). ^{43}Ca was used as internal standards for plagioclase and clinopyroxene, and ^{29}Si was used as internal standard for olivine. BIR-1G was measured during each analytical cycle and was compared with the preferred values reported by Jochum et al. (2005) (Additional file 1: Table S1). Relative standard deviations that are indicative of analytical precision were better than 8% (number of the analyses is 32).

Trace-element concentrations of orthopyroxene were determined at Kanazawa University, using an Agilent 7500S ICP-MS coupled with a MicroLas GeoLas Q-plus 193 nm ArF excimer laser. Analytical method is described in Akizawa et al. (2020). Each analysis was performed by ablating 50 μm in diameter for orthopyroxene. The NIST SRM 614 was measured during each analytical cycle and was compared with the preferred values reported by Morishita et al. (2005) (Additional file 1: Table S1). Relative standard deviations that are indicative of analytical precision were better than 5% (number of the analyses is 6).

6 Results

6.1 Microstructure and CPO

Orientation maps and pole figures of minerals in representative troctolite samples are shown in Figs. 4 and 5. Clinopyroxene orientation map of the coarse-grained troctolite reveals sparse clinopyroxene grains with a similar crystallographic orientation (Fig. 4a, b). Most of the olivine and plagioclase in coarse-grained troctolite as well as skeletal olivine-bearing troctolite show poorly defined CPO (Fig. 5; see also Additional file 2: Fig. S1 for other samples) due to the low number of indexed mineral grains. Plagioclase in relatively fresh coarse-grained troctolites shows a point alignment of planes (010) with a girdle distribution of axes [100] (Fig. 5b). In contrast, the olivine and plagioclase in fine-grained troctolites show well defined CPOs (Fig. 5c, d; see also Additional file 2: Fig. S1 for other samples), where comparatively large areas were indexed (>75% indexed area total; J-index ranges from 1.90 to 12.6 for olivine, and from 1.76 to 6.39 for plagioclase; Table 1). In fine-grained troctolites, the plagioclase CPOs are axial-B type (Fig. 5d), and the

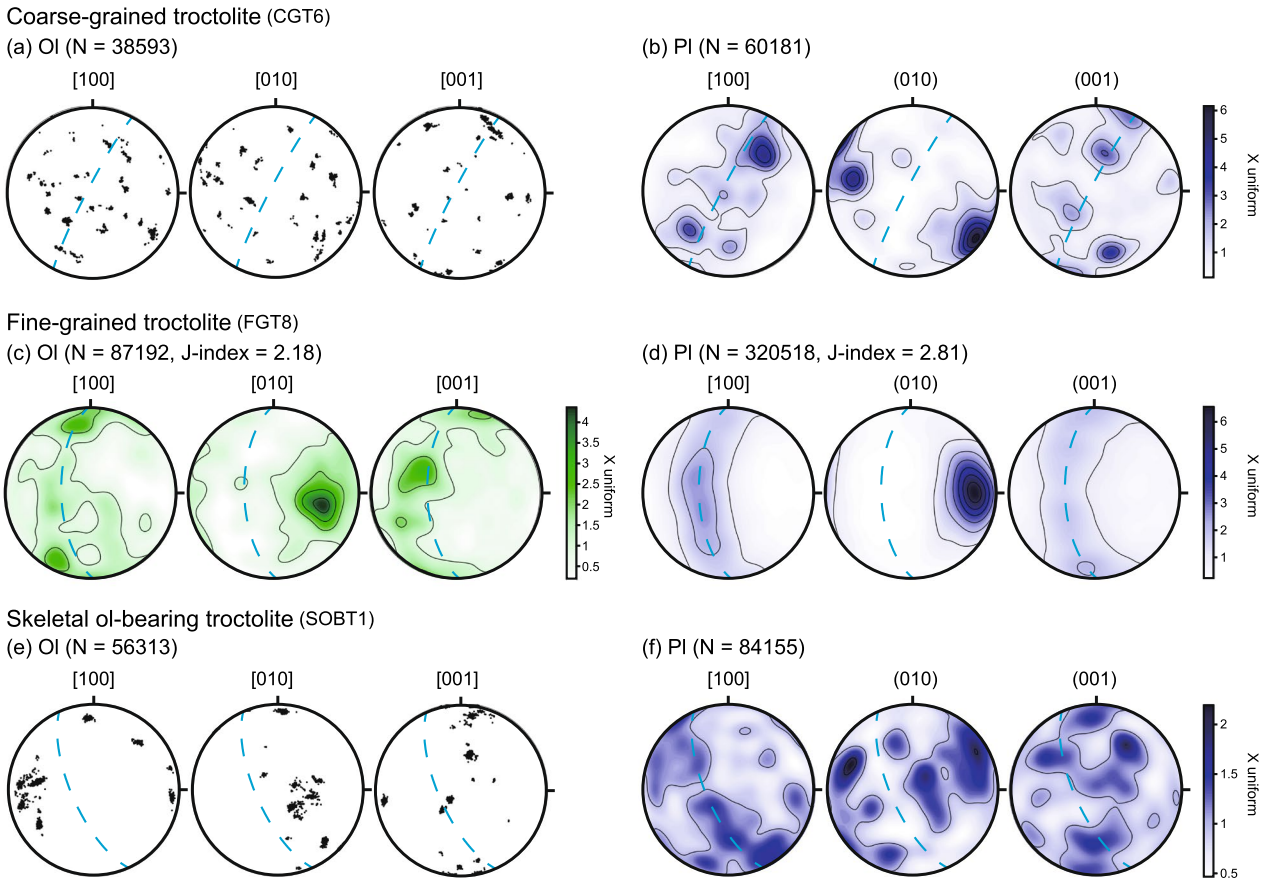

Fig. 5 Pole figures (lower hemisphere) showing CPOs of olivine (left side) and plagioclase (right side) for coarse-grained troctolite (**a**, **b**), fine-grained troctolite (**c**, **d**), and skeletal olivine-bearing troctolite (**e**, **f**). The light-blue dashed lines represent the trace of the foliation defined by the preferred orientation of (010). N represents the number of grains detected by EBSD analysis. *Ol* Olivine, *Pl* Plagioclase

olivine CPOs also show similar crystallographic characteristics; a point alignment of axes [010] with a girdle distribution of axes [100] (Fig. 5c).

6.2 Major-element chemistry

Mean values and all analyzed values of olivine, plagioclase, clinopyroxene, orthopyroxene, and chromian spinel are listed in Additional file 1: Tables S2 to S6. The Hess Deep troctolites show (1) a decrease of Fo value (89–80) and NiO content (0.26–0.12 wt%), and an increase of MnO content (0.12–0.29 wt%) in olivine (Fig. 6a, b), (2) a decrease of An value (89–75) and an increase of FeO content (0.28–0.48 wt%) in plagioclase (Fig. 6c), (3) a decrease of Mg# (0.90–0.83) and Cr_2O_3 content (1.2 to almost nil wt%) in clinopyroxene (Fig. 6d). There are positive correlations between olivine Fo and plagioclase An values (Fig. 7). The coarse-grained troctolites are similar in mineral composition to the most primitive olivine-rich rocks (i.e. plagioclase-bearing dunites from the Hess Deep Rift), whereas the fine-grained and skeletal olivine-bearing troctolites overlap in composition with the gabbroic rocks.

The compositional data of the troctolites from the Atlantis Massif (Mid-Atlantic Ridge) and Atlantis Bank (Southwest Indian Ridge) are shown in Fig. 6. They have compositions distinguishable from the Hess Deep troctolites, with higher olivine NiO content, and lower plagioclase FeO content at the same values of olivine Fo and plagioclase An, respectively (Fig. 6a, c). The values of plagioclase An of the Hess Deep troctolites are much higher than those of the troctolites from the Atlantis Massif and Atlantis Bank at the same values of olivine Fo (Fig. 7).

6.3 Trace-element chemistry

Mean values and all analyzed values of trace element for olivine, plagioclase, clinopyroxene, and orthopyroxene are listed in Additional file 1: Tables S7 to S10. Chondrite-normalized rare-earth element (REE) patterns and primitive mantle-normalized trace-element patterns of olivine, plagioclase, clinopyroxene, and orthopyroxene in the

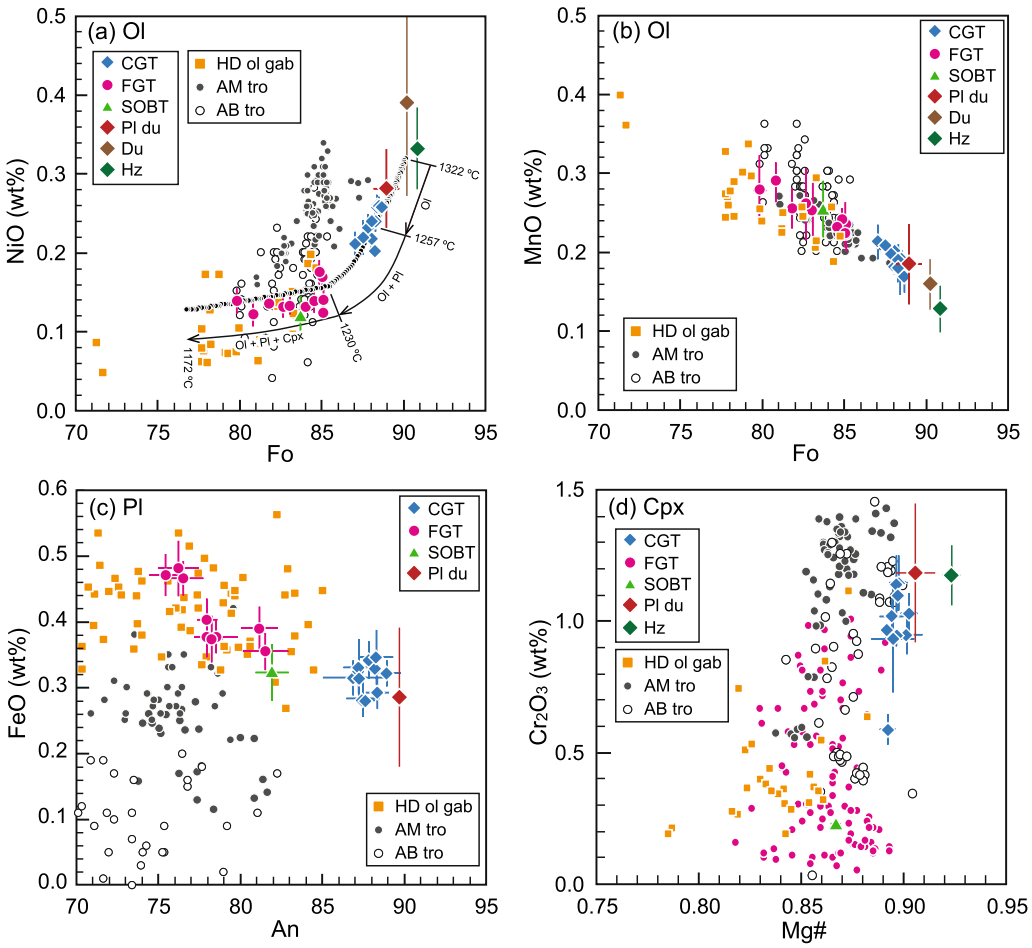

Fig. 6 Chemical compositions of minerals in the troctolites from IODP Site U1415. Each data point represents the mean value of one sample along with measured variability (1 standard deviation). Compositional change during fractional crystallization of primitive MORB melt calculated by rhyolite-MELTS software package is shown by the black dots in (**a**). Calculated data are plotted in each 1 °C decrease. Crystalline mineral pairs are shown. The chemical compositions of plagioclase-bearing dunites, dunites, and harzburgites from Hess Deep are from Arai and Matsukage (1996) and Dick and Natland (1996); those of olivine gabbros from Hess Deep are from Lissenberg et al. (2013); those of troctolites from the Atlantis Bank are from Dick et al. (2002) (data name of OZA and MAE were used herein); and those of troctolites from the Atlantis Massif are from Drouin et al. (2009) and Ferrando et al. (2018). *AB* Atlantis Bank, *AM* Atlantis Massif, *CGT* Coarse-grained troctolite, *Cpx* Clinopyroxene, *Du* Dunite, *FGT* Fine-grained troctolite, *Gab* Gabbro, *HD* Hess Deep, *Hz* Harzburgite, *Ol* Olivine, *Pl* Plagioclase, *Pl du* Plagioclase-bearing dunite, *SOBT* Skeletal olivine-bearing troctolite, *Tro* Troctolite

troctolites are shown respectively in Fig. 8 and Additional file 2: Fig. S2. The olivines display highly fractionated chondrite-normalized REE patterns with a continuous and strong decrease from heavy REE (HREE) to middle REE (MREE), slightly flattening toward light REE (LREE) (Fig. 8a). The plagioclases have LREE-enriched HREE-depleted chondrite-normalized patterns with positive Eu anomaly (Fig. 8b). The chondrite-normalized REE patterns of clinopyroxene show steady moderate depletion from HREE to LREE with a negative Eu anomaly, that is particularly pronounced in the most HREE-rich samples (Fig. 8c, d). The compositional fields for the troctolites from the Atlantis Massif are shown in Fig. 8a–c. The Hess Deep troctolites show REE patterns of olivine, plagioclase and clinopyroxene similar to the Atlantis Massif troctolites. The chondrite-normalized REE patterns of orthopyroxene are characterized by a steady decrease from HREE to LREE with higher concentrations than depleted harzburgites (Fig. 8e).

7 Discussion

7.1 Formation of magmatic porous crystal framework

Plagioclase CPOs of the troctolites from the Hess Deep Rift show typical magmatic fabrics (Fig. 5) with axes [100] and planes (010) of plagioclase parallel to the plane of magmatic flow marked by the tabular shape of the

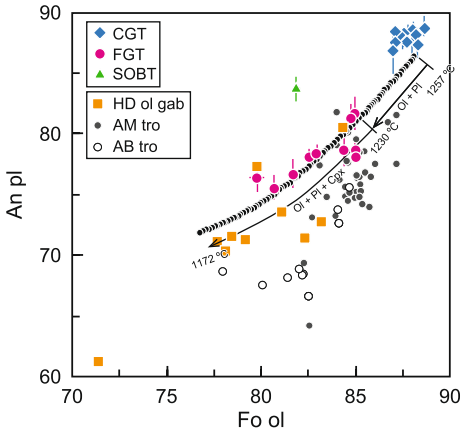

Fig. 7 Compositional variation of olivine Fo and plagioclase An in the troctolites from IODP Site U1415. Each data point represents the mean value of one sample along with measured variability (1 standard deviation). Compositional change during fractional crystallization of primitive MORB melt calculated by rhyolite-MELTS software package is shown by the black dots. Calculated data are plotted in each 1 °C decrease. Crystalline mineral pairs are shown. The chemical compositions of olivine gabbros from Hess Deep are from Lissenberg et al. (2013), those of troctolites from the Atlantis Bank are from Dick et al. (2002) (data name of OZA and MAE were used herein), and those of troctolites from the Atlantis Massif are from Drouin et al. (2009) and Ferrando et al. (2018). Abbreviations are the same as in Fig. 6

plagioclase grain (i.e., axial-B type CPO; Satsukawa et al. 2013). Similar plagioclase CPOs are commonly described in gabbroic rocks from present-day ocean floors as well as in ophiolites (e.g., Lamoureux et al. 1999; Morales et al. 2011; Higgie and Tommasi 2012; Satsukawa et al. 2013; Cheadle and Gee 2017; Basch et al. 2019; Boulanger et al. 2021; Ferrando et al. 2021; Mock et al. 2021). In contrast, compaction of magma-crystal mush also functions to form axial-B type CPO of plagioclase in the lower oceanic crust (e.g., Ferrando et al. 2021). Hence, the fabrics of the Hess Deep troctolites could be controlled not only by the magmatic accretion but also by the compaction in association with mantle flow overturn toward the ocean floor-opening direction (e.g., Boudier and Nicolas 1995).

In the coarse-grained troctolites, clinopyroxenes are sparsely distributed along the grain boundaries of olivine and plagioclase, and share a similar crystallographic orientation at the scale of the thin section (Fig. 4b). The petrographic characteristics corroborate that the clinopyroxenes are connected to each other in three dimension to construct an irregularly prolonged poikilitic clinopyroxene crystal. The presence of such prolonged clinopyroxene crystal recalls previous perspectives that the olivine and plagioclase grains build a porous crystal framework, where the melts continuously migrate along the grain boundaries of olivine and plagioclase in an open system (Philpotts et al. 1999; Philpotts and Dickson 2000; Lissenberg et al. 2013; Lissenberg and MacLeod 2016; Lissenberg et al. 2019; Sanfilippo et al. 2020; Zhang et al. 2021; Ferrando et al. 2021). The pore spaces at the grain boundaries in the coarse-grained troctolites were closing as crystallization proceeded, and the evolving melts saturated with olivine + plagioclase + clinopyroxene probably occupied the connected porous spaces.

7.2 Crystallization process to form troctolites

Chromian spinels enclosed in the olivine and plagioclase grains (Fig. 3a, c, d) are best described by the crystallization of chromian spinel predating the crystallization of olivine and plagioclase. The crystallization of the chromian spinel reduces the Cr_2O_3 content in the residual melts, but the later crystallization mineral, i.e. clinopyroxene contains considerable amounts of Cr_2O_3 up to 1.3 wt% in the coarse-grained troctolites (Fig. 6d). Arai and Matsukage (1998) substantiated that incongruent melting of orthopyroxene in the harzburgite produced the dunite in the Hess Deep Rift, which in turn caused the enrichments of Cr in the ascending melts. This mantle-melt reaction process is expected to leave texturally heterogeneous lithologies in the mantle, such as the plagioclase-bearing dunites drilled at ODP Site 895 (Arai and Matsukage 1996; Boudier et al. 1996; Dick and Natland 1996). The same reaction can be ascribed for the formation of Cr-rich clinopyroxenes in the coarse-grained troctolites. We advocate that the melts filling the porous network along the crystal framework of olivine and plagioclase (see Sect. 7.1) were derived from the mantle after the mantle-melt reactions.

REE compositions of melts in equilibrium with the clinopyroxenes in the troctolites were calculated using the clinopyroxene/melt partition coefficients from Kelemen et al. (2003). Their chondrite-normalized REE patterns are characterized by a steady, yet moderate decrease from HREE to LREE (Fig. 9). In the Ce_{CN}/Dy_{CN} and Sm_{CN}/Dy_{CN} (CN represents chondrite-normalized) space, the compositional area of the melts in equilibrium with the clinopyroxenes overlaps with that of MORB from the EPR (Fig. 10). These compositional features substantiate that the troctolites were crystallized from MORB melts. To constrain the crystallization process of the troctolites from the MORB melts, we conducted thermodynamic modeling using the rhyolite-MELTS software package (Gualda et al. 2012) as described in Appendix. The chemical evolution of primitive MORB melt after Kinzler and Grove (1993) was monitored at 0.2 GPa (~6 km-deep oceanic crust, Frisch et al. 2011) during two possible crystallization processes assuming thermodynamic equilibrium: equilibrium crystallization (crystallized minerals remain in the system and

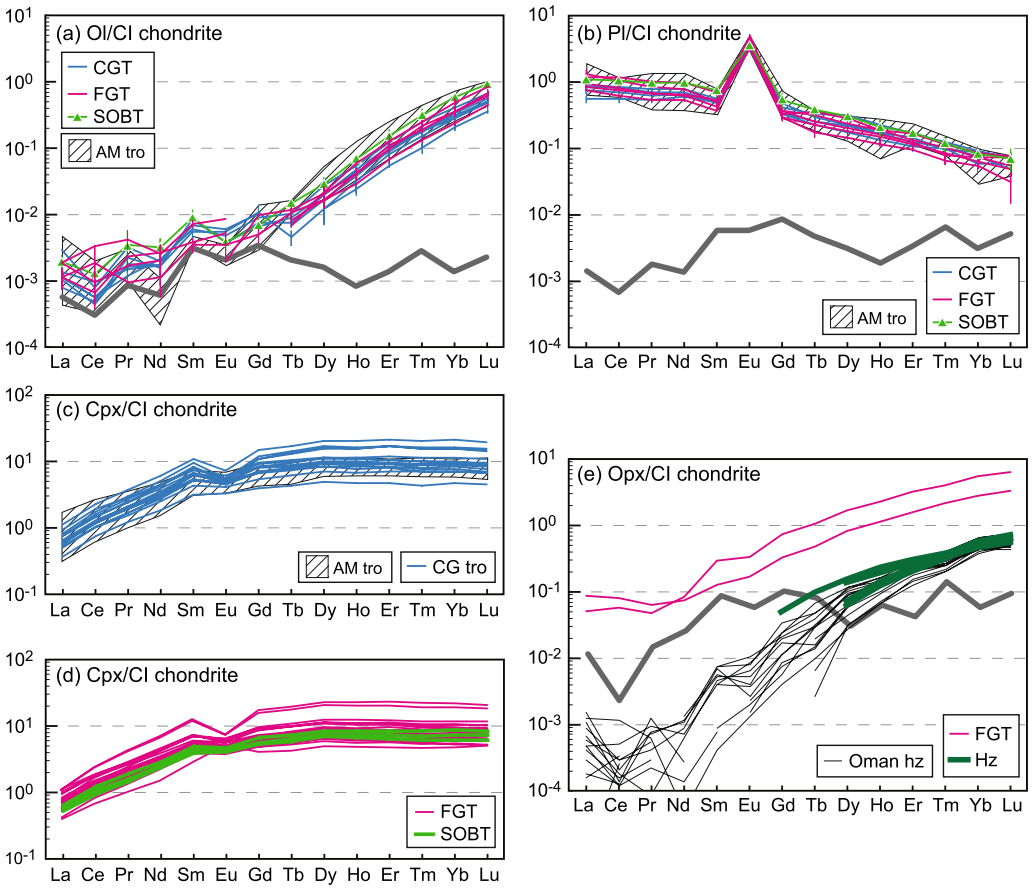

Fig. 8 Chondrite-normalized REE patterns of olivine (**a**), plagioclase (**b**), clinopyroxene (**c**, **d**), and orthopyroxene (**e**) in the troctolites from IODP Site U1415. Each data in **a**, **b** represents the mean value of one sample along with measured variability (1 standard deviation), whereas all data are presented in **c**, **d**, **e**. The compositional fields in **a**, **b**, **c** are of troctolites from the Atlantis Massif from Drouin et al. (2009). The orthopyroxene compositions of the Oman harzburgites in **e** are from Akizawa et al. (2016), (see Additional file 1: Table S11 for compiled data set), and those of the Hess Deep harzburgites are from Grambling et al. (2022). The thick gray lines represent average detection limits of the analyses. Chondrite values are from Sun and McDonough (1989). Abbreviations are the same as in Fig. 6

they are continuously in equilibrium with the residual melt), and fractional crystallization (crystallized minerals are immediately chemically isolated from the system, and they are thus in disequilibrium with the integrated residual melt). The results are presented in Figs. 6a and 7, and Additional file 2: Fig. S3. Decisive defect of the equilibrium crystallization model is that the crystallizing olivines remain constantly high in NiO content even though the melts are highly fractionated (> 0.2 wt% NiO, Additional file 2: Fig. S3). In contrast, the fractional crystallization model can precipitate olivines with low NiO content (< 0.15 wt% NiO; Fig. 6a, Additional file 2: Fig. S3) and duplicate the compositional trend of the olivines in the troctolites and olivine gabbros from the Hess Deep Rift (Fig. 6a). Considering that the chemical compositions of the olivine gabbros are more evolved than the troctolites (Figs. 6a, 7), the former was formed after the latter through a series of the fractional crystallization. The fractional crystallization is the essential process that crystallize the olivine and plagioclase grains in the Hess Deep troctolites.

7.3 Partial dissolution/hybridization processes

Skeletal morphology of olivine has been often reported from layered intrusions and ophiolites, where the skeletal olivine growth was attributed to rapid crystal growth that results from the undercooling of melt and consequent supersaturation in olivine (e.g., Donaldson 1976; Faure et al. 2003, 2007; O'Driscoll et al. 2007; Renna et al. 2016; Basch et al. 2019). The olivine grains are then marked by branching crystal growth as well as their unique "skeletal" morphology. However, the branching olivine crystal growth particular to the layered intrusions was not observed in the Hess Deep skeletal olivine-bearing troctolite (Fig. 3i). In contrast, the olivines in the latter

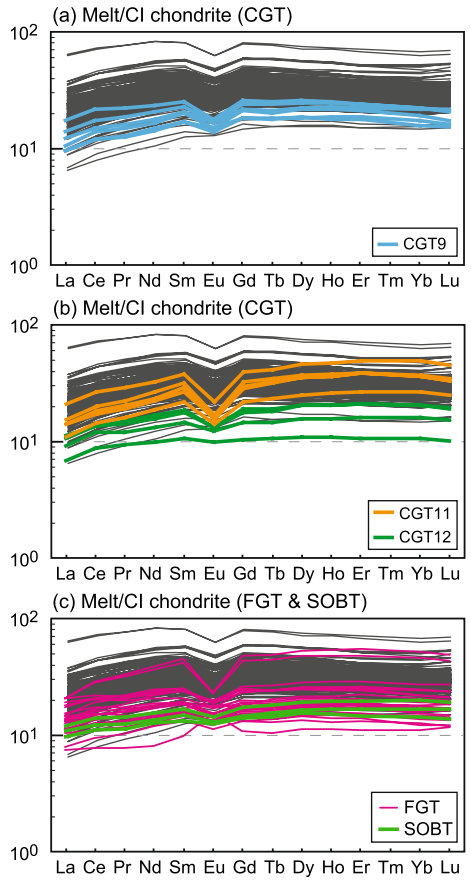

Fig. 9 Chondrite-normalized REE patterns of melt equilibrated with the clinopyroxenes in the troctolites from IODP Site U1415. The melt compositions were calculated using clinopyroxene/melt partition coefficients by Kelemen et al. (2003). Basalt data from Hess Deep are shown by the gray lines (referred from Stewart et al. 2002). Chondrite values are from Sun and McDonough (1989). Abbreviations are the same as in Fig. 6

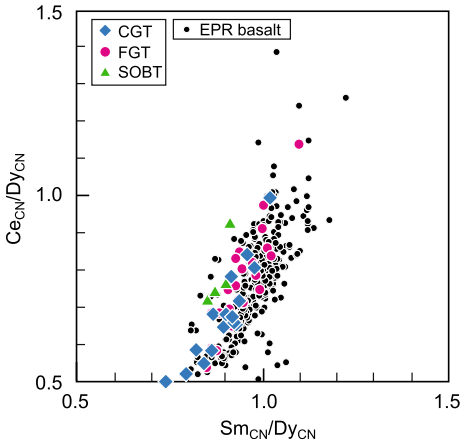

Fig. 10 Compositional variation of chondrite-normalized Ce/Dy and Sm/Dy of calculated melts. CN represents chondrite-normalized. The melt compositions were calculated using clinopyroxene/melt partition coefficients by Kelemen et al. (2003). Basalt data from the EPR are referred from PetDB data base (http://www.earthchem.org/petdb). Chondrite values are from Sun and McDonough (1989). Abbreviations are the same with Fig. 6

show cuspate and embayed margins (Fig. 3i). These petrographic characteristics are interpreted as resulting from olivine dissolution rather than rapid olivine growth (Thornber and Huebner 1985; Tsuchiyama 1986). The mineral dissolution can be induced by mixing of chemically distinct melts (Tsuchiyama 1986), where mineral grains present in one of the source melts is disequilibrated with the newly generated hybridized melt. We argue that the upwelling melts were injected into unsolidified coarse-grained olivine and plagioclase framework and mingled with the interstitial melts (Fig. 11). An abrupt change in melt composition due to melt hybridization probably caused partial dissolution of olivine and plagioclase primocrysts. Considering that the troctolites show magmatic fabrics (see Sect. 7.1), magmatic flow could have probably contributed to the crystal dissolution (convective crystal dissolution; Keer 1995). If the hybridization occurred abruptly, supersaturation produces "skeletal" branching mineral grains (Lofgren and Donaldson 1975). Yet again, such a real skeletal texture is not developed in the skeletal olivine-bearing troctolite. This is probably due to high temperature at the ridge axis; the rate of crystal growth was relatively slow at such a small undercooling region.

7.4 Formation of fine-grained troctolite

Grain size of the fine-grained troctolite is finer (~2 mm in diameter) than the coarse-grained and skeletal olivine-bearing troctolites (~10 mm in diameter). Considering the smaller grain size, the fine-grained troctolite was most probably crystallized with high crystallization rate attained by hotter melt injection into a colder wall rock. Leuthold et al. (2018) substantiated this idea: the clinopyroxene oikocrysts in the fine-grained troctolites were formed after cumulus gabbro experienced partial melting by newly injected hot melts followed by complex hybridization/crystallization process of the partial melt and the injected melt. With reflecting this complex hybridization/crystallization history, the clinopyroxene oikocrysts show wide ranges of chemical composition (ca. nil to 1 wt% Cr_2O_3 and 0.82 to 0.90 Mg#, Fig. 6d), and the olivine grains are abundant (Fig. 2b, Table 1) irrespective of their evolved chemical composition (Fig. 6a).

To quantify thermal condition during the fine-grained troctolite formation, we used the REE-in-plagioclase-clinopyroxene thermometer formulated by Sun and Liang (2017) and the two-pyroxene thermometer formulated by Brey and Köhler (1990). We used the rim composition of the clinopyroxene oikocryst, where the chemical

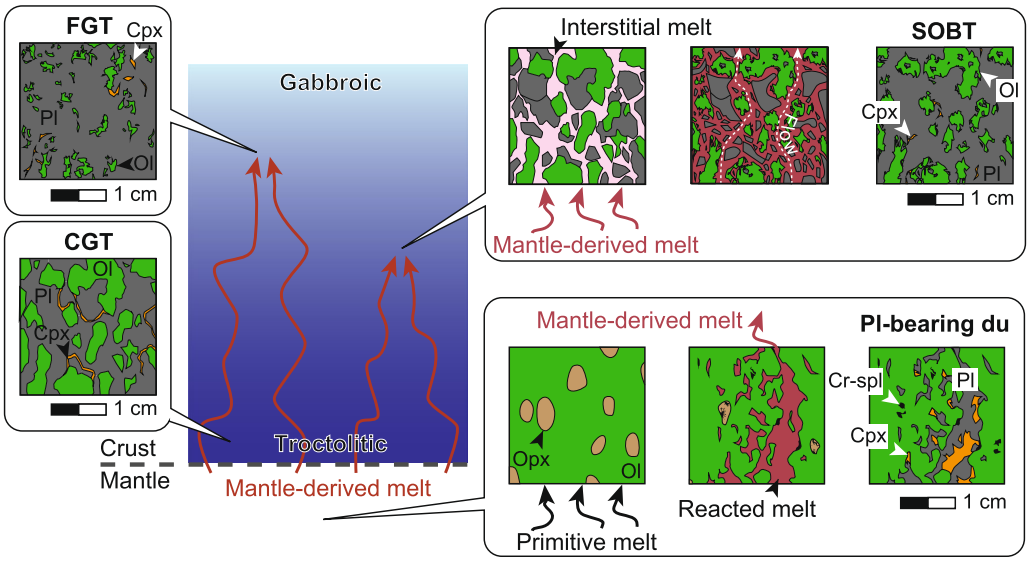

Fig. 11 Illustration of troctolite and dunite formations beneath the Hess Deep Rift. See text for the details. *CGT* Coarse-grained troctolite, *Cr-spl* Chromian spinel, *Cpx* Clinopyroxene, *Du* Dunite, *FGT* Fine-grained troctolite, *Ol* Olivine, *Opx* Orthopyroxene, *Pl* Plagioclase, *SOBT* Skeletal olivine-bearing troctolite

equilibrium with the plagioclase and orthopyroxene can be expected. The pressure was set at 0.2 GPa corresponding to ~ 6 km-deep oceanic crust (e.g., Frisch et al. 2011). The results show that the temperature ranges from 1182 to 1245 °C with the former thermometer (T_{REE}), and from 901 to 1059 °C with the later thermometer (T_{BKN}) (Table 1). The T_{REE} are much higher than T_{BNK} (Table 1). This is because the major divalent cation (Mg^{2+} and Fe^{2+})-based thermometer likely does not record the initial crystallization temperature due to faster subsolidus diffusive re-equilibration of the divalent cations in comparison with the REE (Sun and Liang (2017), and references therein). Hence, the formation temperature of the fine-grained troctolite can be estimated to be ca. 1205 °C (mean value of the above mentioned T_{REE}). In comparison, Leuthold et al. (2018) estimated the formation temperature of the clinopyroxene oikocryst at 1205 °C with the temperature of the wall gabbro at 1000 °C, using an isenthalpic assimilation model. These formation temperatures are in good agreement, substantiating the concurrent formation of the fine-graine troctolite and clinopyroxene oikocryst. This is reinforced by our thermodynamic model results that the olivine, plagioclase, and clinopyroxene were coprecipitated in the fine-grained troctolite (Figs. 6a, 7). As the temperature of the wall gabbro was estimated to be relatively cold (e.g., 1000 °C, Leuthold et al. 2018), the level where the fine-grained troctolites were crystallized was relatively shallower than the levels where the coarse-grained and skeletal olivine-bearing troctolites were emplaced (Fig. 11).

The fine-grained troctolites contain small amounts of orthopyroxene in close association with the olivine (Fig. 3h). Similarly, orthopyroxene-bearing gabbroic rocks have been reported in the IODP Expedition 345 cores (Gillis et al. 2014b). The crystallization of the orthopyroxene was interpreted either as evidence of fractionation to crystallize orthopyroxene, shallow mantle melting (e.g., O'Hara 1968), or re-equilibration of parental melts with shallow mantle without significant mixing with aggregated melts in the lower crust level (Coogan et al. 2002). However, the fine-grained troctolites are not evolved enough to precipitate orthopyroxene (Figs. 6a, 7) and the orthopyroxenes are not equilibrated with those in the mantle harzburgites (Fig. 8e). Instead, we argue that the peritectic reaction between olivine and evolved melt generated by the partial melting of gabbro precursor: the dissolution of olivine at rim and the nucleation with growth of orthopyroxene in the evolved melt boundary layer (Zellmer et al. 2016). Such two-step process of olivine dissolution and orthopyroxene growth can explain the limited presence of the orthopyroxene rimming the olivine grain (Fig. 3h).

8 Summary and conclusions

Microstructural and mineral chemical data on the troctolite suite recovered during IODP Expedition 345 suggest the following scenario for evolutional process of the lower crust at Hess Deep. Primitive melts ascending through the uppermost mantle reacted with adjoining wall harzburgites. Olivine-rich lithologies such as

dunite and plagioclase-bearing dunite were left as reaction products along the melt path in the mantle. The mantle-derived melts constructed a framework of coarse-grained (~ 10 mm) olivine and plagioclase via in-situ fractional crystallization when they intruded into the lower crust level. Porous space along the grain boundaries were gradually closing as crystallization proceeded, and was occupied by evolved melt that eventually crystallized clinopyroxene. The mantle-derived primitive melts thus variously fractionated forming coarse-grained troctolites and olivine gabbros. The evolved lower crust was injected by the mantle-derived primitive melts, which mingled with interstitial evolved melts already present along the grain boundaries of fractionated olivine and plagioclase framework. Hybridized melts were consequently in chemical disequilibrium with the olivine and plagioclase primocrysts. The abrupt change in composition of the hybridized melt as well as magmatic flow caused partial dissolution of the olivine and plagioclase primocrysts; hence, the preexisting olivine and plagioclase grains were segregated into olivine and plagioclase grains with a skeletal habit (formation of skeletal olivine-bearing troctolites). In contrast, when injected into a colder and more evolved gabbroic wall rock, the hybridized melts crystallized with high crystallization rate, which led to the formation of the fine-grained troctolite and to the local crystallization of orthopyroxene. The chemical variation of the skeletal olivine-bearing and fine-grained troctolites was probably balanced by the complex hybridization/crystallization processes.

Appendix

The compositional evolutions of MORB melts were monitored in the process of batch crystallization (equilibrium crystallization) or fractional crystallization using a thermodynamic model of rhyolite-MELTS (Gualda et al. 2012). Primary MORB melt inferred after Kinzler and Grove (1993) was chosen as a starting source material: 46.0 wt% SiO_2, 0.74 wt% TiO_2, 17.9 wt% Al_2O_3, 8.47 wt% FeO, 13.4 wt% MgO, 11.8 wt% CaO, 0.06 wt% K_2O, 1.72 wt% Na_2O, and 0.033 wt% NiO. The crystallizing pressure was fit at 0.2 GPa (suitable pressure at the crust/mantle boundary) and oxygen fugacity (fO_2) at the quartz-fayalite-magnetite buffer.

Abbreviations

CGT	Coarse-grained troctolite
CPO	Crystallographic preferred orientation
EBSD	Electron backscatter diffraction
EPR	East Pacific Rise
FGT	Fine-grained troctolite
HREE	Heavy rare-earth element
LREE	Light rare-earth element
MORB	Mid-ocean ridge basalt
MREE	Middle rare-earth element
ODF	Orientation distribution function
REE	Rare-earth element
SOBT	Skeletal olivine-bearing troctolite

Supplementary Information

The online version contains supplementary material available at https://doi.org/10.1186/s40645-023-00560-4.

Additional file 1. Supplementary tables.

Additional file 2. Supplementary figures.

Acknowledgements

This research used samples and data provided by the International Ocean Discovery Program. We wish to express our deep thanks to all members of the shipboard scientific party, marine technicians and specialists, and the captain and crew of JOIDES Resolution for their collaboration, kindness and friendship during IODP Expedition 345. We are grateful to T. Morishita for daily discussions, C. Nevado and D. Delmas for the production of high-quality thin sections, F. Barou for his assistance with EBSD analysis, and O. Bruguier and A. Tamura for their assistance with LA-ICP-MS analyses. This manuscript was improved by valuable comments from two anonymous reviewers.

Author contributions

NA and BI carried out structural analyses, and NA and MG conducted chemical analyses of the samples. SA collaborated in the construction of this manuscript. All the authors read and approved the final version of this manuscript.

Funding

The funding for this research was provided by a grant from the Japan Agency for Marine-Earth Science and Technology (JAMSTEC). NA was supported by JSPS program Grant Number R2404, strategic young researcher overseas visits program for accelerating brain circulation (provided to SA), for visiting University of Montpellier to make structural and chemical analyses. NA was also supported by JSPS KAKENHI Grant Number JP23H01267.

Availability of data and materials

Supplementary figures are available as Additional file 2: Figs. S1 to S3, and supplementary dataset is given in Additional file 1: Tables S1 to S11.

Declarations

Competing interests

The authors declare that they have no competing interest.

Received: 24 October 2022 Accepted: 1 June 2023
Published online: 15 June 2023

References

Akizawa N, Ozawa K, Tamura A, Michibayashi K, Arai S (2016) Three-dimensional evolution of melting, heat and melt transfer in ascending mantle beneath a fast-spreading ridge segment constrained by trace elements in clinopyroxene from concordant dunites and host harzburgites of the Oman ophiolite. J Petrol 57:777–814. https://doi.org/10.1093/petrology/egw020

Akizawa N, Früh-Green FL, Tamura A, Tamura C, Morishita T (2020) Compositional heterogeneity and melt transport in mantle beneath Mid-Atlantic Ridge constrained by peridotite, dunite, and wehrlite from Atlantis Massif. Lithos 245–355:105364. https://doi.org/10.1016/j.lithos.2019.105364

Arai S, Matsukage K (1996) Petrology of the gabbro-troctolite-peridotite complex from Hess Deep, equatorial Pacific: implications for mantle-melt interaction within the oceanic lithosphere. In: Mével C, Gillis KM, Allan JF

(eds) Proceedings of the ocean drilling program. Scientific Results, vol 147. College Stain, Texas, pp 135–155
Arai S, Matsukage K (1998) Petrology of a chromitite micropod from Hess Deep, equatorial Pacific: a comparison between abyssal and alpine-type podiform chromitites. Lithos 43:1–14. https://doi.org/10.1016/S0024-4937(98)00003-6
Arai S, Takemoto Y (2007) Mantle wehrlite from Hess Deep as a crystal cumulate from an ultra-depleted primary melt in East Pacific Rise. Geophys Res Lett 34:L08302. https://doi.org/10.1029/2006GL029198
Basch V, Rampone E, Crispini L, Ferrando C, Ildefonse B, Godard M (2019) Multi-stage reactive formation of troctolites in slow-spreading oceanic lithosphere (Erro–Tobbio, Italy): a Combined Field and Petrochemical Study. J Petrol 60:873–906. https://doi.org/10.1093/petrology/egz019
Bachmann F, Hielscher R, Schaeben H (2010) Texture analysis with MTEX–free and open source software toolbox. Solid State Phenom 160:63–68. https://doi.org/10.4028/www.scientific.net/SSP.160.63
Blackman DK, Ildefonse B, John BE, Ohara Y, Miller DJ, Abe N et al (2011) Drilling constraints on lithospheric accretion and evolution at Atlantis Massif, Mid-Atlantic Ridge 30° N. J Geophys Res 116:B07103. https://doi.org/10.1029/2010JB007931
Boudier F, Nicolas A (1995) Nature of the Moho transition zone in the Oman ophiolite. J Petrol 36:777–796. https://doi.org/10.1093/petrology/36.3.777
Boudier F, MacLeod CJ, Bolou L (1996) Structures in peridotites from Site 895, Hess Deep: implications for the geometry of mantle flow beneath the East Pacific Rise. In: Mével C, Gillis KM, Allan JF (eds) Proceedings of the ocean drilling program. Scientific Results, vol 147. College Stain, Texas, pp 347–356
Boulanger M, France L, Ferrando C, Ildefonse B, Ghosh B, Sanfilippo A, Liu C-Z, Morishita T, Koepke J, Bruguier O (2021) Magma-mush interactions in the lower oceanic crust: Insights from Atlantis Bank layered series (Southwest Indian Ridge). J Geophys Res Solid Earth. https://doi.org/10.1029/2021jb022331
Brey GP, Köhler T (1990) Geothermobarometry in four-phase lherzolites II. New thermobarometers, and practical assessment of existing thermobarometers. J Petrol 31:1353–1378. https://doi.org/10.1093/petrology/31.6.1353
Bunge HJ (1982) Texture analysis in materials sciences. Buttleworth, London
Cannat M, Chatin F, Whitechurch H, Ceuleneer G (1997) Gabbroic rocks trapped in the upper mantle at the Mid-Atlantic Ridge. In: Karson JA, Cannat M, Miller DJ, Elthon D (eds) Proceedings of the ocean drilling program. Scientific Results, vol 153. College Stain, Texas, pp 243–264
Cheadle MJ, Gee JS (2017) Quantitative textural insights into the formation of gabbro in mafic intrusions. Elements 13:409–414. https://doi.org/10.2138/gselements.13.6.409
Collier M, Kelemen PB (2010) The case of reactive crystallization at mid-ocean ridges. J Petrol 51:1913–1940. https://doi.org/10.1093/petrology/egq043
Coogan LA, Gillis KM, MacLeod CJ, Thompson GM, Hékinian R (2002) Petrology and geochemistry of the lower ocean crust formed at the East Pacific Rise and exposed at Hess Deep: a synthesis and new results. Geochem Geophys Geosyst 13:8604. https://doi.org/10.1029/2001GC000230
Davis AS, Clague DA (1990) Gabbroic xenoliths from the northern Gorda Ridge: implications for magma chamber processes under slow spreading centers. J Geophys Res 95:10885–10905
De Paolo DJ (1981) Trace element and isotopic effects of combined wallrock assimilation and fractional crystallization. Earth Planet Sci Lett 53:189–202. https://doi.org/10.1016/0012-821X(81)90153-9
Dick HJB, Natland JH (1996) Late-stage melt evolution and transport in the shallow mantle beneath the East Pacific Rise. In: Mével C, Gillis KM, Allan JF (eds) Proceedings of the ocean drilling program. Scientific Results, vol 147. College Stain, Texas, pp 103–134
Dick HJB, Natland JH, Alt JC, Bach W, Bideau D, Gee JS, Haggas S, Hertogen JGH, Hirth G, Holm PM, Ildefonse B, Iturrino GJ, John BE, Kelley DS, Kikawa E, Kingdon A, LeRoux PJ, Maeda J, Meyer PS, Miller DJ, Naslund HR, Niu Y-L, Robinson PT, Snow J, Stephen RA, Trimby PW, Worm H-U, Yoshinobu A (2000) A long in situ section of the lower ocean crust: results of ODP Leg 176 drilling at the Southwest Indian Ridge. Earth Planet Sci Lett 179:31–51. https://doi.org/10.1016/S0012-821X(00)00102-3
Dick HJB, Ozawa K, Meyer PS, Niu Y, Robinson PT, Constantin M, Hebert R, Maeda J, Natland JH, Hirth JG, Mackie SM (2002) Primary silicate mineral chemistry of a 1.5 km section of very slow spreading lower ocean crust: ODP Hole 735B, Southern Indian Ridge. In: Natland JH, Dick HJB, Miller DJ, Von Herzen RP (eds) Proceedigs of the ocean drilling program. Scientific Results, vol 176. College Stain, Texas, pp 1–61
Dick HJB, Tivey MA, Tucholke BE (2008) Plutonic foundation of a slow-spreading ridge segment: oceanic core complex at Kane Megamullion, 23°30′N, 45°20′W. Geochem Geophys Geosyst 9:Q05014. https://doi.org/10.1029/2007GC001645
Dixon JE, Clague DA, Eissen J-P (1986) Gabbroic xenoliths and host ferrobasalt from the southern Juan de Fuca Ridge. J Geophys Res 91:3795–3820. https://doi.org/10.1029/JB091iB03p03795
Donaldson CH (1976) An experimental investigation of olivine morphology. Contrib Mineral Petrol 57:187–213
Drouin M, Godard M, Ildefonse B, Bruguier O, Garrido CJ (2009) Geochemical and petrographic evidence for magmatic impregnation in the oceanic lithosphere at Atlantis Massif, Mid-Atlantic Ridge (IODP Hole U1309D, 30°N). Chem Geol 264:71–88. https://doi.org/10.1016/j.chemgeo.2009.02.013
Drouin M, Ildefonse B, Godard M (2010) A microstructural imprint of melt impregnation in slow spreading lithosphere: olivine-rich troctolites from the Atlantis Massif, Mid-Atlantic Ridge, 30°N, IODP Hole U1309D. Geochem Geophys Geosyst 11:Q06003. https://doi.org/10.1029/2009GC002995
Elthon D (1987) Petrology of gabbroic rocks from the Mid-Cayman Rise spreading center. J Geophys Res 92:658–682. https://doi.org/10.1029/JB092iB01p00658
Faure F, Trolliard G, Nicollet C, Montel J-M (2003) A developmental model of olivine morphology as a function of the cooling rate and the degree of undercooling. Contrib Mineral Petrol 145:251–263. https://doi.org/10.1007/s00410-003-0449-y
Faure F, Schiano P, Trolliard G, Nicollet C, Soulestin B (2007) Textural evolution of polyhedral olivine experiencing rapid cooling rates. Contrib Mineral Petrol 153:405–416. https://doi.org/10.1007/s00410-006-0154-8
Ferrando C, Godard M, Ildefonse B, Rampone E (2018) Melt transport and mantle assimilation at Atlantis Massif (IODP Site U1309): Constraints from geochemical modeling. Lithos 323:24–43. https://doi.org/10.1016/j.lithos.2018.01.012
Ferrando C, Lynn KJ, Basch V, Ildefonse B, Godard M (2020) Retrieving timescales of oceanic crustal evolution at Oceanic Core Complexes: Insights from diffusion modelling of geochemical profiles in olivine. Lithos 105727:376–377. https://doi.org/10.1016/j.lithos.2020.105727
Ferrando C, Basch V, Ildefonse B, Deans J, Sanfilippo A, Barou F, France L (2021) Role of compaction in melt extraction and accumulation at a slow spreading center: Microstructures of olivine gabbros from the Atlantis Bank (IODP Hole U1473A, SWIR). Tectonophysics 815:229001. https://doi.org/10.1016/j.tecto.2021.229001
Ferrini VL, Shillington D, Gillis K, MacLeod CJ, Teagle DAH, Morris A, Cazenave PW, Hurst S, Tominaga M, the JC21 Scientific Party (2013) Evidence of mass failure in the Hess Deep Rift from multi-resolutional bathymetry data. Mar Geol 339:3–21. https://doi.org/10.1016/j.margeo.2013.03.006
Francheteau J, Armijo R, Cheminée JL, Hekinian R, Lonsdale P, Blum N (1990) 1 Ma East Pacific Rise oceanic crust and uppermost mantle exposed by rifting in Hess Deep (equatorial Pacific Ocean). Earth Planet Sci Lett 101:281–295. https://doi.org/10.1016/0012-821X(90)90160-Y
Francheteau J, Armijo R, Cheminee JL, Hekinian R, Lonsdale P, Blum N (1992) Dyke complex of the East Pacific Rise exposed in the walls of Hess Deep and the structure of the upper oceanic crust. Earth Planet Sci Lett 111:109–121. https://doi.org/10.1016/0012-821X(92)90173-S
Freund S, Beier C, Krumm S, Haase KM (2013) Oxygen isotope evidence for the formation of andesitic–dacitic magmas from the fast-spreading Pacific-Antarctic Rise by assimilation–fractional crystallisation. Chem Geol 347:271–283. https://doi.org/10.1016/j.chemgeo.2013.04.013
Frisch W, Meschede M, Blakey R (eds) (2011) Plate tectonics: continental drift and mountain building. Springer, Berlin
Gillis KM, Mèvel C, Allan J et al (1993) Proceedings of the ocean Drilling Program, Initial Reports, vol 147. College Station, Texas
Gillis KM, Snow JE, Klaus A, the Expedition 345 Scientists (2014a) Proceedings of the Ocean Drilling Program. Initial Report, vol. 345. College Station, Texas
Gillis KM, Snow JE, Klaus A, Abe N, Adrião ÁB, Akizawa N, Ceuleneer G, Cheadle MJ, Faak K, Falloon TT, Friedman SA, Godard M, Guerin G, Harigane Y, Horst AJ, Hoshide T, Ildefonse B, Jean MM, John BE, Koepke J, Machi S,

Maeda J, Marks NE, McCaig AM, Meyer R, Morris A, Nozaka T, Python M, Saha A, Wintsch RP (2014b) Primitive layered gabbros from fast-spreading lower oceanic crust. Nature 505:204–207. https://doi.org/10.1038/nature12778

Girardeau J, Francheteau J (1993) Plagioclase-wehrlites and peridotites on the east Pacific Rise (Hess Deep) and the Mid-Atlantic Ridge (DSDP Site 334): evidence for magma percolation in the oceanic upper mantle. Earth Planet Sci Lett 115:137–149. https://doi.org/10.1016/0012-821X(93)90218-X

Godard M, Awaji S, Hansen H, Hellebrand E, Brunelli D, Johnson K, Yamasaki T, Maeda J, Abratis M, Christie D, Kato Y, Mariet C, Rosner M (2009) Geochemistry of a long in-situ section of intrusive slow-spread oceanic lithosphere: results from IODP Site U1309 (Atlantis Massif, 30ºN Mid-Atlantic-Ridge). Earth Planet Sci Lett 279:110–122. https://doi.org/10.1016/j.epsl.2008.12.034

Grambling NL, Dygert N, Boring B, Jean MM, Kelemen PB (2022) Thermal history of lithosphere formed beneath fast spreading ridges: Constraints from the mantle transition zone of the East Pacific Rise at Hess Deep and Oman Drilling Project, Wadi Zeeb, Samail Ophiolite. J Geophys Res Solid Earth 127:e2021JB022696. https://doi.org/10.1029/2021JB022696

Grove TL, Kinzler RJ, Bryan WB (1993) Fractionation of mid-ocean ridge basalt (MORB). In: Morgan JP et al (eds) Mantle flow and melt generation at mid-ocean ridges, Geophys Monogr Ser 71. AGU, Washington D.C., pp 281–310

Gualda GAR, Ghiorso MS, Lemons RV, Carley TL (2012) Rhyolite-MELTS: a Modified calibration of MELTS optimized for silica-rich, fluid-bearing magmatic systems. J Petrol 53:875–890. https://doi.org/10.1093/petrology/egr080

Günther D, Heinrich CA (1999) Enhanced sensitivity in laser ablation-ICP mass spectrometry using helium-argon mixture as aerosol carrier. J Anal Spectrom 14:1363–1368. https://doi.org/10.1039/A901648A

Higgie K, Tommasi A (2012) Feedbacks between deformation and melt distribution in the crust–mantle transition zone of the Oman ophiolite. Earth Planet Sci Lett 359–360:61–72. https://doi.org/10.1016/j.epsl.2012.10.003

Hekinian R, Bideau D, Francheteau J, Cheminee JL, Armijo R, Lonsdale P, Blum N (1993) Petrology of the East Pacific Rise crust and upper mantle exposed in Hess Deep (eastern equatorial pacific). J Geophys Res 98:8069–8094. https://doi.org/10.1029/92JB02072

Herzberg C (2004) Geodynamic information in peridotite petrology. J Petrol 45:2507–2530. https://doi.org/10.1093/petrology/egh039

Hielscher R, Schaeben H (2008) A novel pole figure inversion method: specification of the MTEX algorithm. J Appl Crystallogr 41:1024–1037. https://doi.org/10.1107/S0021889808030112

Jochum KP, Nohl U, Herwig K, Lammel E, Stoll B, Hofmann AW (2005) GeoReM: a new geochemical database for reference materials and isotopic standards. Geostand Geoanal Res 29:333–338. https://doi.org/10.1111/j.1751-908X.2005.tb00904.x

Karson JA, Hurst SD, Lonsdale P (1992) Tectonic rotation of dikes in fast-spread oceanic crust exposed near Hess Deep. Geology 20:685–688. https://doi.org/10.1130/0091-7613(1992)020%3c0685:TRODIF%3e2.3.CO;2

Kelemen PB, Yogodzinski GM, Scholl DW (2003) Along-strike variation in the Aleutian Island Arc: genesis of high Mg# andesite and implications for continental crust. In: Eiler J (ed) Inside the Subduction Factory. Geophysical Monograph, vol. 138. American Geophysical Union, Washington, pp 223–276

Keer RC (1995) Convective crystal dissolution. Contrib Mineral Petrol 121:237–246. https://doi.org/10.1007/BF02688239

Kinzler RJ, Grove TL (1993) Correction and further discussion of the primary magmas of mid-ocean ridge basalts, 1 and 2. J Geophys Res 98:2339–22347. https://doi.org/10.1029/93JB02164

Lamoureux G, Ildefonse B, Mainprice D (1999) Modelling the seismic properties of fast-spreading ridge crustal low-velocity zones: insights from Oman gabbro textures. Techtonophysics 312:283–301. https://doi.org/10.1016/S0040-1951(99)00183-3

Leuthold J, Lissenberg CJ, O'Driscoll B, Karakas O, Falloon T, Klimentyeva DN, Ulmer P (2018) Partial melting of lower oceanic crust gabbro: constraints from poikilitic clinopyroxene primocrysts. Front Earth Sci 6:15. https://doi.org/10.3389/feart.2018.00015

Lissenberg CJ, MacLeod CJ, Howard KA, Godard M (2013) Pervasive melt migration through fast-spreading lower oceanic crust (Hess Deep, equatorial Pacific Ocean). Earth Planet Sci Lett 361:436–447. https://doi.org/10.1016/j.epsl.2012.11.012

Lissenberg CJ, MacLeod CJ (2016) A reactive porous flow control on mid-ocean ridge magmatic evolution. J Petrol 57:2195–2220. https://doi.org/10.1093/petrology/egw074

Lissenberg CJ, MacLeod CJ, Bennet EN (2019) Consequences of a crystal mush-dominated magma plumbing system: a mid-ocean ridge perspective. Phil Trans R Soc A 377:20180014. https://doi.org/10.6084/m9.figshare.c.4302707

Lofgren GE, Donaldson CH (1975) Curved branching crystals and differentiation in comb-layered rocks. Contrib Mineral Petrol 49:309–319. https://doi.org/10.1007/BF00376183

Lonsdale P (1988) Structural pattern of the Galapagos microplate and evolution of the Galapagos triple junctions. J Geophys Res 93:13551–13574. https://doi.org/10.1029/JB093iB11p13551

Mainprice D, Silver PG (1993) Interpretation of SKS-waves using samples from the subcontinental lithosphere. Phys Earth Planet Interiors 78:257–280. https://doi.org/10.1016/0031-9201(93)90160-B

Mainprice D, Bachmann F, Hielscher R, Schaeben H (2015) Descriptive tools for the analysis of texture projects with large datasets using MTEX: strength, symmetry and components. In: Faulkner DR, Mariani E, Mecklenburgh J (eds) Rock deformation from field, experiments and theory: a volume in honour of Ernie Rutter. Special Publications, vol 409, Geological Society, London, pp 251–271. https://doi.org/10.1144/SP409.8

Michael PJ, Schilling J-G (1989) Chlorine in mid-ocean ridge magmas: evidence for assimilation of seawater-influenced components. Geochim Cosmochim Acta 53:3131–3143. https://doi.org/10.1016/0016-7037(89)90094-X

Mock D, Ildefonse B, Müller T, Koepke J (2021) A reference section through fast-spread lower oceanic crust, Wadi Gideah, Samail Ophiolite (Sultanate of Oman): insights from crystallographic preferred orientations. J Geophys Res Solid Earth. https://doi.org/10.1029/2021jb021864

Morales LFG, Boudier F, Nicolas A (2011) Microstructures and crystallographic preferred orientation of anorthites from Oman ophiolite and the dynamics of melt lenses. Tectonics 30:TC2011. https://doi.org/10.1029/2010TC002697

Morishita T, Ishida Y, Arai S, Shirasaka M (2005) Determination of multiple trace element compositions in thin (<30 μm) layers of NIST SRM 614 and 616 using laser abulation-inductively couples plasma-mass spectrometry (LA-ICP-MS). Geostand Geoanal Res 29:107–122. https://doi.org/10.1111/j.1751-908X.2005.tb00659.x

O'Driscoll B, Donaldson C, Troll VR, Jerram DA, Emeleus H (2007) An origin for harrisitic and granular olivine in the Rum layered suite, NW Scotland: a crystal size distribution study. J Petrol 48:253–270. https://doi.org/10.1093/petrology/egl059

O'Hara MJ (1968) Are ocean floor basalts primary magma? Nature 220:683–685

Pearce NJG, Perkins WT, Westgate JA, Gorton MP, Jackson SE, Neal CR, Chenery SP (1997) A compilation of new and published major and trace element data for NIST SRM 610 and NIST SRM 612 glass reference materials. Geostandard Newslett 21:115–144. https://doi.org/10.1111/j.1751-908X.1997.tb00538.x

Perk NW, Coogan LA, Karsin JA, Klein EM, Hanna HD (2007) Petrology and geochemistry of primitive lower oceanic crust from Pito Deep: implications for the accretion of the lower crust at the southern East Pacific Rise. Contrib Mineral Petrol 154:575–590. https://doi.org/10.1007/s00410-007-0210-z

Philpotts AR, Brustman CM, Shi J, Carlson WD, Denison C (1999) Plagioclase-chain networks in slowly cooled basaltic magma. Am Min 84:1819–1829

Philpotts AR, Dickson LD (2000) The formation of plagioclase chains during convective transfer in basaltic magma. Nature 406:59–61. https://doi.org/10.1038/35017542

Prior DJ, Mariani E, Wheeler J (2009) EBSD in the earth sciences: applications, common practice, and challenges. In: Schwartz AJ, Kumar M, Adams BL, Field DP (eds) Electron backscatter diffraction in materials science. Springer, Boston, pp 345–360. https://doi.org/10.1007/978-0-387-88136-2

Renna MR, Tribuzio R, Ottolini L (2016) New perspectives on the origin of olivine-rich troctolites and associated harrisites from the Ligurian ophiolites (Italy). J Geol Soc 173:916–932. https://doi.org/10.1144/jgs2015-135

Ridley WI, Perfit MR, Smith MC, Fornari DJ (2006) Magmatic processes in developing oceanic crust revealed in a cumulate xenolith collected at the East Pacific Rise, 9º50'N. Geochem Geophys Geosyst 7:Q12O04. https://doi.org/10.1029/2006GC001316

Rioux M, Lissenberg CJ, McLean NM, Bowring SA, MacLeod CJ, Hellebrand E, Shimizu N (2012) Protracted timescales of lower crustal growth at the fast-spreading East Pacific Rise. Nat Geosci 5:275–278. https://doi.org/10.1038/ngeo1378

Sanfilippo A, MacLeod CJ, Tribuzio R, Lissenberg CJ, Zanetti A (2020) Early-stage melt-rock reaction in a cooling crystal mush beneath a slow-spreading mid-ocean ridge (IODP Hole U1473A, Atlantis Bank, Southwest Indian Ridge). Front Earth Sci 8:554598. https://doi.org/10.3389/feart.2020.579138

Satsukawa T, Ildefonse B, Mainprice D, Morales LFG, Michibayashi K, Barou F (2013) A database of plagioclase crystal preferred orientations (CPO) and microstructures; implications for CPO origin, strength, symmetry and seismic anisotropy in gabbroic rocks. Solid Earth 4:511–542. https://doi.org/10.5194/se-4-511-2013

Schaeben H (1999) The de la Vallée Poussin standard orientation density function. Textures Microstruct 33:365–373. https://doi.org/10.1155/TSM.33.365

Schmidt N-H, Olesen N (1989) Computer-aided determination of crystal-lattice orientation from electron-channeling patterns in the SEM. Can Min 27:15–22

Skemer P, Katayama I, Jiang Z, Karato S-I (2005) The misorientation index: development of a new method for calculating the strength of lattice-preferred orientation. Tectonophysics 411:157–167. https://doi.org/10.1016/j.tecto.2005.08.023

Smith MC, Perfit MR, Jonasson IR (1994) Petrology and geochemistry of basalts from the southern Juan de Fuca Ridge: controls on the spatial and temporal evolution of mid-ocean ridge basalt. J Geophys Res 99:4787–4812. https://doi.org/10.1029/93JB02158

Stewart MA, Klein EM, Karson JA (2002) Geochemistry of dikes and lavas from the north wall of the Hess Deep Rift: insights into the four-dimensional character of crustal construction at fast-spreading mid-ocean ridges. J Geophys Res 107:2238. https://doi.org/10.1029/2001JB000545

Sun C, Liang Y (2017) A REE-in-plagioclase–clinopyroxene thermometer for crustal rocks. Contrib Mineral Petrol 172:24. https://doi.org/10.1007/s00410-016-1326-9

Sun SS, McDonough WF (1989) Chemical and isotopic systematics of oceanic basalts: implications for mantle composition and processes. In: Saunders AD, Norry MJ (eds) Magmatism in the Ocean Basins, Special Publication, vol 42. Geological Society, London, pp 313–345

Thornber CR, Huebner JS (1985) Dissolution of olivine in basaltic liquids: experimental observations and applications. Am Min 70:934–945

Tsuchiyama A (1986) Melting and dissolution kinetics: application to partial melting and dissolution of xenoliths. J Geophys Res 91:9395–9406. https://doi.org/10.1029/JB091iB09p09395

Van Achterbergh E, Ryan CG, Jackson SE, Griffin WL (2001) Data reduction software for LA-ICP-MS. In: Sylvester PJ (ed) Laser ablation-ICP-mass spectrometry in the Earth Sciences. Short Course Series, vol 29, Mineralogical Association of Canada, Québec, pp 239–243

Vanko DA, Batiza R (1982) Gabbroic rocks from the Mathematician Ridge failed rift. Nature 300:742–744. https://doi.org/10.1038/300742a0

Zellmer GF, Sakamoto N, Matsuda N, Iizuka Y, Moebis A, Yurimoto H (2016) On progress and rate of the peritectic reaction Fo + SiO_2 → En in natural andesitic arc magmas. Geochim Cosmochim Acta 185:383–393. https://doi.org/10.1016/j.gca.2016.01.005

Zhang W-Q, Dick HJB, Liu C-Z, Lin Y-Z, Amgeloni LM (2021) MORB melt transport through Atlantis Bank oceanic batholith (SW Indian Ridge). J Petrol 62:1–35. https://doi.org/10.1093/petrology/egab034

Publisher's Note